

# Light-matter entanglement over 50 km of optical fibre

V. Krutyanskiy<sup>†,1</sup>, M. Meraner<sup>†,1,2</sup>, J. Schupp<sup>†,1,2</sup>,  
V. Krcmarsky<sup>1,2</sup>, H. Hainzer<sup>1,2</sup> and B. P. Lanyon<sup>1,2,\*</sup>

<sup>1</sup>*Institut für Quantenoptik und Quanteninformation,*

*Österreichische Akademie der Wissenschaften, Technikerstr. 21A, 6020 Innsbruck, Austria*

<sup>2</sup>*Institut für Experimentalphysik, Universität Innsbruck, Technikerstr. 25, 6020 Innsbruck, Austria*

When shared between remote locations, entanglement opens up fundamentally new capabilities for science and technology. Envisioned quantum networks use light to distribute entanglement between their remote matter-based quantum nodes. Here we report on the observation of entanglement between matter (a trapped ion) and light (a photon) over 50 km of optical fibre: two orders of magnitude further than the state of the art and a practical distance to start building large-scale quantum networks. Our methods include an efficient source of ion-photon entanglement via cavity-QED techniques (0.5 probability on-demand fibre-coupled photon from the ion) and a single photon entanglement-preserving quantum frequency converter to the 1550 nm telecom C band (0.25 device efficiency). Modestly optimising and duplicating our system would already allow for 100 km-spaced ion-ion heralded entanglement at rates of over 1 Hz. We show therefore a direct path to entangling 100 km-spaced registers of quantum-logic capable trapped-ion qubits, and the optical atomic clock transitions that they contain.

## INTRODUCTION

Envisioned quantum networks [1] consist of distributed matter-based quantum nodes, for the storage, manipulation and application of quantum information, which are interconnected with photonic links to establish entanglement between the nodes. While the most ambitious form of a quantum network is a collection of remote quantum computers, far simpler networks with a handful of qubits at each node could already enable powerful applications in quantum enhanced distributed sensing, timekeeping, cryptography and multiparty protocols [2].

Entanglement has been achieved between two atoms in traps a few ten meters apart [3], between two ions in traps a few meters apart [4] and recently between two nitrogen-vacancy centres 1.3 km apart [5]. In these experiments, photon-matter entanglement is first generated, then detection of one or two photons heralds remote matter-matter entanglement (entanglement is “swapped” from matter-light to matter-matter). A current goal is to significantly scale up the distance over which quantum matter can be entangled to a hundred kilometres or more, which are practical internode spacings to enable large-scale quantum networks.

Some key challenges to entangling matter over such distances are now described. First, the aforementioned matter systems emit photons at wavelengths that are strongly absorbed in optical waveguides (such as optical fibre), limiting the internode distance to a few kilometers. For example, in the present work 854 nm photons are collected from a trapped atomic ion. While the  $\sim 3$  dB/km losses suffered by 854 nm photons through state-of-the-

art optical fibre allows for few kilometre internode distances, transmission over 50 km of fibre would be  $10^{-15}$ . Single-photon quantum frequency conversion to the telecom C band (1550 nm) would offer a powerful solution: this wavelength suffers the minimum fibre transmission losses ( $\sim 0.18$  dB/km, yielding 10 % transmission over 50 km) and is therefore an ideal choice for a standard interfacing wavelength for quantum networking. Photons from solid-state memories [6], cold gas memories [7, 8], quantum dots and nitrogen-vacancy centres [9] have been converted to telecom wavelengths. Frequency conversion of photons from ions has very recently been performed, including to the telecom C band (without entanglement) [10], to the telecom O band with entanglement over 80 m [11] and directly to an atomic Rubidium line at 780 nm [12]. The use of photon conversion to extend the distance over which light-matter and matter-matter entanglement can be distributed has not previously been achieved.

A second challenge to long distance matter entanglement is to preserve entanglement when such long photonic channels are involved. Uncontrolled decoherence processes that act on the photon as it travels along its path, and those that act on the quantum matter during the photon travel time, can easily destroy entanglement. For example, the entanglement-carrying photon signal, which attenuates exponentially with distance in any lossy waveguide, can be overwhelmed by added photon noise from the photon frequency conversion process or dark counts of the photon detectors. The inter-node photon travel time also imposes a minimum coherence time for matter, which for e.g. 50 km of optical fibre is already significant at 250  $\mu$ s (and 500  $\mu$ s to allow for the classical signal of a successful herald to return). Moreover, quantum networking applications require distributed entanglement of a quality above certain thresholds, for which the required matter coherence times and photon signal

---

\* [ben.lanyon@uibk.ac.at](mailto:ben.lanyon@uibk.ac.at),<sup>†</sup> These authors contributed equally

to noise ratio are far more challenging.

A third challenge comes again from the photon travel time. The shortest time required to entangle remote matter (or indeed light) in two places is the light travel time between them. The 500  $\mu\text{s}$  wait time over 50 km of optical fibre yields a maximum attempt rate of only 2 kHz: one must wait 500  $\mu\text{s}$  to learn if an individual attempt to distribute remote entanglement has been successful. To achieve practical entanglement distribution rates in the face of such a restriction, one can work on achieving a high probability for individual attempts to succeed and (or) to run many attempts in parallel (as discussed later).

In this work, entanglement between a trapped-ion qubit and a photon that has travelled over 50 km of optical fibre is achieved. The quality of the entanglement is sufficiently high to allow for a clear violation of a Bell inequality — as required for some of the most challenging device-independent quantum network applications [13]. Furthermore, when modestly optimised, the achieved rate is expected to allow for entanglement distribution between 100 km-spaced trapped ions at rates over 1 Hz. The paper is organised as follows. First, there is a short motivation for quantum networking trapped ions. Second, a brief overview of the experimental methods is given, with much detail left for the supplementary material. Third, the tomographically-reconstructed entangled state, of the ion qubit and photon polarisation qubit after 50 km, is presented and the achieved fidelity, efficiency and rate are analysed. Fourth, the ion qubit is shown to provide a quantum information storage time (coherence time) of more than 20 ms, allowing for future entanglement distribution over thousands of kilometers. Finally, the prospects for 100 km ion-ion entanglement are presented as well as a path to significantly increase the rate via multi-mode and hybrid quantum networking.

Trapped ions are particularly powerful systems to enable quantum networking and the envisioned applications. For example, a complete set of tools for deterministic universal manipulation of quantum information encoded into registers of trapped ions is readily available and of a quality near fault tolerant thresholds [14–16], as required for arbitrary distance quantum networking via the quantum repeater approach [17, 18]. Key quantum networking functionalities have been demonstrated between ions over a few meters, including remote state teleportation [19] and multi-ion protocols [20]. Trapped ions are also some of the most sensitive measurement probes yet developed. For example, many ion species, including the one used in this work, contain optical atomic clock transitions and therefore entangling them over distance enables the ideas presented in [21] and [22] to be explored.

## RESULTS

Our network node consists of a  $^{40}\text{Ca}^+$  ion in a radio-frequency linear Paul trap with an optical cavity that

enhances photon collection on the 854 nm electronic dipole transition. (Figure 1). A Raman laser pulse at 393 nm triggers emission, by the ion, of a photon into the cavity via a bichromatic cavity-mediated Raman transition (CMRT) [23]. Two indistinguishable processes are driven in the CMRT, each leading to the generation of a cavity photon and resulting in entanglement between photon polarisation and the electronic qubit state of the ion of the form  $1/\sqrt{2} (|D_{J=5/2, m_j=-5/2}, V\rangle + |D_{J=5/2, m_j=-3/2}, H\rangle)$ , with horizontal ( $H$ ) and vertical ( $V$ ) photon polarisation and two metastable Zeeman states of the ion ( $D_J, m_j$ ) [24]. The total measured probability of obtaining an on-demand free-space photon out of the ion vacuum chamber (entangled with the ion) is  $P_{out} = 0.5 \pm 0.1$  [24], enabled by the novel low-loss cavity in our setup.

The CMRT yields an entangled state with a frequency-degenerate photon qubit (the two polarisation components have the same frequency to within the cavity linewidth [23]), providing a significant benefit for long distance networking: the phase of the light-matter entangled state does not depend on the time at which the photon detection event occurs at a given distance from the ion. Photon detection time fluctuates due to the intrinsic finite temporal extent of the photon wavepacket and in the case of optical path length changes, which could be significant over tens of kilometres of deployed optical fibre. Our photons are generated over several tens of microseconds, with a corresponding bandwidth of tens of kilohertz. This unusually narrow bandwidth allows for strong frequency filtering, which we exploit in the photon conversion process and could have further benefits in future deployed networks, e.g to enable co-propagating classical and quantum light. Furthermore, the corresponding photon coherence-length is potentially thousands of meters, allowing for essentially path-length-insensitive entanglement swapping between remote ions via Hong-Ou-Mandel interference [4, 25, 26].

Single-mode fibre-coupled photons from the ion are injected into a polarisation-preserving photon conversion system (previously characterised using classical light [27]). In summary, a  $\chi^{(2)}$  optical nonlinearity is used to realise difference frequency generation, whereby the energy of the 854 nm photon is reduced by that of a pump-laser photon at 1902 nm, yielding 1550 nm. Two commercially-available free-space and crossed PPLN ridge waveguide crystals are used, one to convert each polarisation, in a self-stable polarisation interferometer. The total fibre-coupled device conversion efficiency here is  $25 \pm 0.02\%$ , for an added white noise of 40 photons/s, within the filtering bandwidth of 250 MHz centred at 1550 nm. As discussed in [27], the 854 nm line in  $^{40}\text{Ca}^+$  is almost unique amongst trapped-ion transitions in its potential for low-noise, highly-efficient single-step frequency conversion to the telecom C band.

Following conversion, the telecom photon is injected into a 50.47 km ‘SMF28’ single-mode fibre spool with 0.181 dB/km loss ( $10.4 \pm 0.5\%$  measured total transmis-

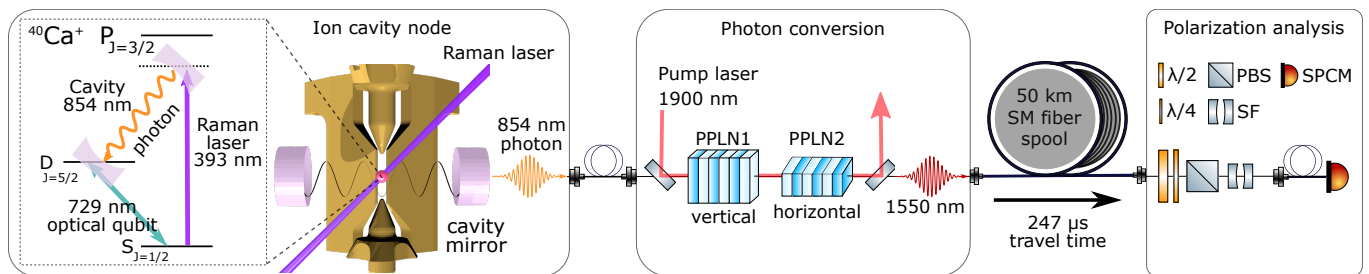


FIG. 1. **Simplified experiment schematic.** From left to right: A single atomic ion (red sphere) in the centre of a radio-frequency linear Paul trap (gold electrodes) and a vacuum anti-node of an optical cavity. A Raman laser pulse triggers emission of an 854 nm photon into the cavity, which exits to the right. The photon, polarisation-entangled with two electronic qubit states of the ion (two Zeeman states of the  $D_{J=5/2}$  manifold, not shown), is then wavelength-converted to 1550 nm using difference frequency generation involving ridge-waveguide-integrated periodically-poled lithium niobate (PPLN) chips and a strong ( $\sim 1$  W) pump laser at 1902 nm [27]. The photon then passes through a 50 km single-mode fibre spool, is filtered with a 250 MHz bandwidth etalon (SF) to reduce noise from the conversion stage [27], and is polarisation-analysed using waveplates, a polarising beam splitter (PBS) and a solid-state single photon counting module (SPCM, InGaAs ID230 from IDQuantique). The electronic state of the ion is measured (not shown), conditional on the detection of a photon. Additional photon conversion filters are not shown [27]. For further details see [24].

sion probability). The spool is not actively stabilised. Polarisation dynamics in an unspooled fibre could be actively controlled using methods developed in the field of quantum cryptography (e.g. [28]). Finally, free-space projective polarisation analysis is performed and the photon is detected using a telecom solid-state photon detector with an efficiency of  $0.10 \pm 0.01$  and free-running dark count rate of 2 cps. Measurement of the ion-qubit state is performed conditional on the detection of a 50 km photon within a 30  $\mu\text{s}$  time window: the Zeeman ion qubit is mapped into the established  $^{40}\text{Ca}^+$  optical quadrupole clock qubit [29] via laser pulses at 729 nm, followed by standard fluorescence state detection (see Methods).

Quantum state tomography is performed to reconstruct the two-qubit (ion qubit and photon polarisation qubit) state [24]. The 247  $\mu\text{s}$  photon travel time through the fibre limits the maximum attempt rate for generating a photon from the ion to 4 kHz (2 kHz if the fibre was stretched out away from our ion to force an additional delay for the classical signal ‘photon click’ to return). Here, until photon detection occurs, photon generation (Raman laser pulses are) performed every 453  $\mu\text{s}$ , yielding an attempt rate of 2.2 kHz. For the complete experimental sequence see Methods. All error bars on quantities derived from the tomographically-reconstructed states (density matrices) are based on simulated uncertainties due to finite measurement statistics [24].

A strongly entangled ion-photon state is observed (Figure 2) over 50 km, quantified by a concurrence [30]  $C=0.75 \pm 0.05$  and state fidelity  $F^m=0.86 \pm 0.03$  with a maximally entangled state ( $C=1$ ). Simulating a CHSH Bell inequality test [31] on our tomographic data yields a value of  $2.304 \pm 0.125$ , thereby exceeding the classical bound (of 2) by 2.4 standard deviations. Using a shorter detection window (first 2/3 of the full photon wavepacket) increases the signal to noise ratio and yields  $F^m=0.90 \pm 0.03$  and CHSH Bell inequality violation by

4.8 standard deviations at the expense of an efficiency decrease of only 10%. The quality of our light-matter entangled state therefore surpasses this stringent threshold for its subsequent application.

For a detailed analysis of the sources of infidelity in the entangled state see [24]; here now is a short summary. In a second experiment, the telecom entangled state is reconstructed right after the conversion stage (without the 50 km spool), yielding  $F^m=0.92 \pm 0.02$ . The drop in fidelity when adding the 50 km spool can, to within statistical uncertainty, be entirely explained by our telecom photon detector dark counts (2 cps). In a third experiment, the 854 nm entangled state is reconstructed right out of the vacuum chamber (without conversion), yielding  $F^m=0.967 \pm 0.006$ . The observed drop in fidelity through the conversion stage alone is dominated by a drop in photon signal to noise signal. Here the noise consists of comparable rates of telecom detector dark counts and conversion noise (caused by Anti-Stokes Raman scattering of the pump laser [27]) and the signal is reduced by the finite conversion setup efficiency and the lower telecom detector’s efficiency compared to the 854 nm one. The infidelity in the 854 nm photon-ion entangled state is consistent with that achieved in [23].

The total probability that a Raman pulse led to the detection of a photon after 50 km was  $P = 5.3 \times 10^{-4}$ , which given an attempt rate of 2.2 kHz yielded a click rate of  $\approx 1$  cps. Photon loss mechanisms in our experiment are discussed in [24]. In summary, the 50 km fibre transmission (0.1) and our current telecom detector efficiency (0.1) limit the maximum click probability to  $P = 0.01$ . The majority of other losses are in passive optical elements, and could largely be eliminated by e.g. more careful attention to coupling into optical fibres and photon conversion waveguides. In combination with state-of-the-art telecom detectors (efficiency 0.9 for  $< 5$  dark cps), a total 50 km efficiency of  $P \approx 0.01$  would be

expected and a corresponding click rate of  $\approx 20$  cps.

One of the functions played by matter in a quantum network is as a memory to store established entanglement, while entanglement is being made or processed in other parts of the network. Decoherence processes in the matter qubit will limit the distance over which it is possible to distribute quantum entanglement (the distance a photon could possibly travel in the ‘coherence time’ of the matter qubit). In our 50 km experiment, the ion qubit is already stored for the 250  $\mu\text{s}$  photon travel time through the 50 km fibre, with no statistically significant reduction in the ion-photon entanglement quality<sup>1</sup>.

Additional tomographic measurements are performed to see for how long ion-photon entanglement could be stored in our ion-trap network node before decoherence in the ion-qubit would destroy it. Specifically, state tomography is performed for increasing delays introduced between measurements of the telecom photon polarisation state (0 km fibre travel distance) and measurements of the state of the ion-qubit. This is equivalent to introducing an additional storage time for the ion-qubit. The results show that strong entanglement is still present after 20 ms wait time ( $F^m = 0.77 \pm 0.04$ ,  $C = 0.57 \pm 0.08$ ), the longest wait time employed. This already opens up the possibility of distributing entanglement over several thousands of kilometers and the time to perform hundreds of single and multi-qubit ion quantum logic gates [32].

A dominant source of decoherence of our ion-qubit are uncontrolled fluctuating energy-level shifts due to intensity fluctuations of the 806 nm laser field used to lock the cavity around the ion. Further attention to minimising the absolute size of these fluctuations should lead to entanglement storage times of more than  $\approx 100$  ms and therefore the possibility to distribute entanglement to the other side of the earth. Beyond this, the ion-qubit could be transferred to hyperfine clock transitions within different co-trapped ion species that offer coherence times of many seconds and longer [33].

## DISCUSSION

The rates for future 100 km-spaced photon-detection heralded ion-ion entanglement using our methods are now discussed (see Figure 3). A modestly optimised version of our system is considered, that achieves an on-demand 50 km photon click probability of  $P = 0.01$  and operates at an attempt rate of  $R = 2$  kHz (the two-way light travel time). By duplicating our experiment, and following a two-photon click heralding scheme [25], the probability of heralding a 100 km spaced ion-ion entangled state would be  $H_2 = \frac{1}{2}P^2 = 5 \times 10^{-5}$ , at an average

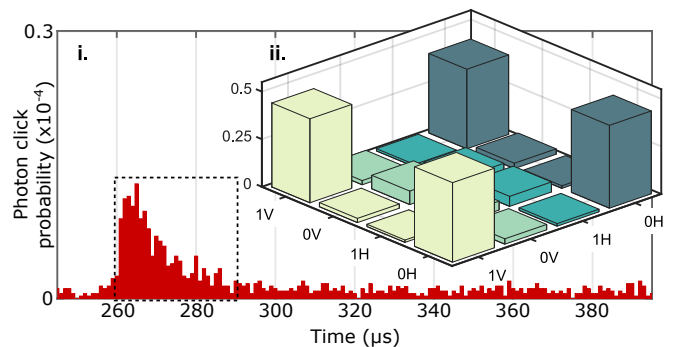


FIG. 2. **Observation of ion-photon entanglement over 50 km of optical fibre.** **i.** 2D red bar chart: histogram of photon detection times (photon wavepacket in dashed box), following the generation of an 854 nm photon with a 30  $\mu\text{s}$  Raman laser pulse (R)  $\approx 250$   $\mu\text{s}$  earlier, repeated at 2.2 kHz. Ion-photon state tomography is performed for photon detection events recorded in the dashed box (total contained probability  $P = 5.3 \times 10^{-4}$ ). **ii.** 3D bar chart: absolute value of experimentally-reconstructed density matrix of the telecom photonic polarisation qubit ( $H$  and  $V$  are Horizontal and Vertical, respectively) and ion-qubit state ( $|0\rangle = |D_{J=5/2, m_j=-3/2}\rangle$ ,  $|1\rangle = |D_{J=5/2, m_j=-5/2}\rangle$ ).

click rate of  $H_2 \times R = 0.1$  cps (comparable with the first rates achieved over a few meters [34] of 0.03 cps). Following a single-photon click scheme [25], one finds  $H_1 = 2P \times 0.1 = 0.002$ , and an average click rate of 2 cps, where 0.1 is the reduced photon generation probability at each node (as required for this scheme). This factor 20 improvement over the two-photon scheme comes at the expense of the need to interferometrically stabilise the optical path length across the 100 km network. The threshold value  $P > 0.04$  for which  $H_2 > H_1$  is within reach with our setup, when allowing for recently-developed 0.16 dB/km loss telecom C band fibres.

An approach to significantly increase the remote entanglement heralding rate is multi-mode quantum networking, where many photons are sent, each entangled with different matter qubits. In this way, of running many such processes in parallel, the probability of at least one successful heralding event occurring can be made arbitrarily high. In our setup, for example, multiple ions can be trapped and it may be possible to produce a train of photons, each entangled with a different ion. In this case, a higher rate of photon production can be employed, as the time between photons in the train is not limited by the light travel time. Furthermore, multi-mode networking could be realised using inhomogeneously-broadened ensemble based solid state quantum memories [35]. Such memories could be quantum-networked with ions via a photon conversion interface [36] to form a powerful hybrid system for long distance quantum networking.

The 50 km photon in our experiments is entangled with the 729 nm optical-qubit clock transition in  $^{40}\text{Ca}^+$ , over which a fractional frequency uncertainty of  $1 \times 10^{-15}$  has been achieved (comparable with the Cs standard) [37]. Furthermore,  $^{40}\text{Ca}^+$  can be co-trapped with  $\text{Al}^+$  [38],

<sup>1</sup> This was achieved by installing a mu-metal shield around the ion-trap vacuum chamber to attenuate ambient magnetic field fluctuations.

which contains a clock transition for which a fractional systematic frequency uncertainty at the  $1 \times 10^{-18}$  level was recently achieved [39, 40]. Transfer of the remote  $^{40}\text{Ca}^+$  entanglement to a co-trapped  $\text{Al}^+$  ion could be done via quantum logic techniques [40, 41]. As such, our work provides a direct path to realise entangled networks of state-of-the-art atomic clocks over large distances [21]. Entangling clocks provides a way to perform more sensitive measurements of their average ticking frequencies [21] and to overcome current limits to their synchronisation [22].

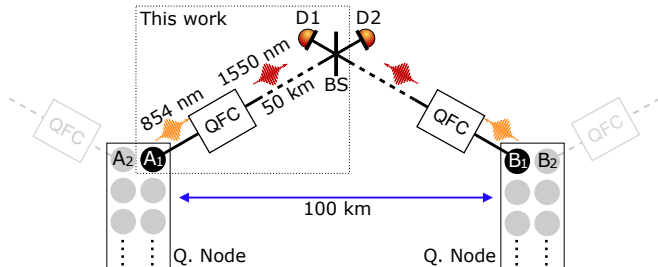


FIG. 3. **Path to 100 km matter-matter entanglement.**

This work: quantum frequency conversion (QFC) converts a photon, emitted on-demand from and entangled with an ion qubit ( $A_1$ ) in node A, to the telecom C band at 1550 nm. The photon then travels through 50 km of optical fibre before detection (D1 or D2). Future work: duplicating the system, interfering the two photonic channels on a beamsplitter (BS). Single or two photon detection heralds the projection of ions  $A_1$  &  $B_1$  into an entangled state [25]. Deterministic intra-node quantum logic and measurement between e.g.  $B_1$  &  $B_2$  and  $A_1$  &  $A_2$  can swap the entanglement over larger distances (quantum repeater). Additional qubits in nodes are available for entanglement purification. Nodes could as well contain solid-state memories [36], NV centres [9] or neutral atoms [7, 8].

## METHODS

### A. Trapped ion node

We use a 3D radio-frequency linear Paul trap with a DC endcap to ion separation of 2.5 mm and ion to blade distance of 0.8 mm. The trap electrodes are made of titanium, coated with gold and are mounted on Sapphire holders. The trap drive frequency is 23.4 MHz. The radial secular frequencies are  $\omega_x \approx \omega_y = 2\pi \times 2.0$  MHz, split by approximately 10 kHz and the axial frequency is  $\omega_z = 2\pi \times 0.927$  MHz. Atoms are loaded from a resistively heated atomic oven and ionised via a two photon process involving 375 nm and 422 nm laser light.

The optical cavity around the ion is near-concentric with a length  $l = 19.9057 \pm 0.0003$  mm and radii of curvature  $ROC = 9.9841 \pm 0.0007$  mm, determined from simultaneous measurements of the free spectral range

(FSR) and higher-order TEM mode spacing (assuming identical mirror geometries) [42]. From this we calculate an expected cavity waist of  $\omega_0 = 12.31 \pm 0.07$   $\mu\text{m}$  and a maximum ion-cavity coupling rate of  $g_{max} = 2\pi \cdot 1.53 \pm 0.01$  MHz. The finesse of the cavity (at 854 nm) is  $\mathcal{F} = \frac{2\pi}{\mathcal{L}} = 54000 \pm 1000$ , with the total cavity losses  $\mathcal{L} = T_1 + T_2 + L_{1+2} = 116 \pm 2$  ppm, determined from measurements of the cavity ringdown time. This gives the cavity linewidth  $2\kappa = 2\pi \cdot 140 \pm 3$  kHz,  $\kappa$  being the half-width at half maximum. Taking into account the spontaneous scattering rate of the  $P_{3/2}$  state of the ion ( $\gamma = 2\pi \cdot 11.45$  MHz, half width) the expected cooperativity is  $C = \frac{g_{max}^2}{2\kappa\gamma} = 1.47 \pm 0.03$ . The transmission  $T_{1,2}$  of our cavity mirrors<sup>2</sup> was measured to be  $T_1 = 2.2 \pm 0.3$  ppm,  $T_2 = 97 \pm 4$  ppm, that yields expected probability of extracting a photon from the cavity of  $P_{out}^{max} = T_2 / (T_1 + T_2 + L_{1+2}) = 0.83 \pm 0.03$ .

The optical cavity axis is close to perpendicular to the principle ion trap axis (approximately  $5^\circ$  difference). A magnetic field of 4.22 G is applied perpendicular to the cavity axis and at an angle of 45 degrees to the principle ion trap axis (supplementary Figure S.4). The Raman photon generation beam is circularly polarised and parallel to the magnetic field (to maximise the coupling on the relevant dipole transition  $S_{J=1/2, m_j=-1/2} \leftrightarrow P_{J=3/2, m_j=-3/2}$ , see supplementary Figure S.6).

### B. Pulse sequence for 50 km experiment

First, a  $30 \mu\text{s}$  ‘initialisation’ laser pulse at 393 nm is applied, measured by a photodiode in transmission of the ion-trap chamber, which allows for intensity stabilisation of the subsequent 393 nm photon generation Raman pulse via a sample and hold system. The initialisation pulse is followed by a  $1500 \mu\text{s}$  Doppler cooling pulse.

Next, a loop starts in which single photons are generated (see supplementary Fig S.5). This loop consists of an additional Doppler cooling pulse ( $50 \mu\text{s}$ ), optical pumping to the  $S = S_{J=1/2, m_j=-1/2}$  state via circularly polarised 397 nm ‘sigma’ laser light ( $60 \mu\text{s}$ ), and a 393 nm photon generation Raman pulse ( $30 \mu\text{s}$ ). This is followed by a wait time for the photon to travel through the 50 km fibre and a subsequent photon detection window. This sequence loops until a photon is detected.

In the case of a photon detection (detector ‘click’), the state of the ion is measured. To perform an ion state measurement, the  $D_I = D_{J=5/2, m_j=-5/2}$  electron population is first mapped to the  $S = S_{J=1/2, m_j=-1/2}$  state via a 729 nm  $\pi$  pulse (supplementary Fig. S.5, Fig S.6). That is, the D-manifold qubit is mapped into an optical qubit (with logical states  $S = S_{J=1/2, m_j=-1/2}$

<sup>2</sup> Polishing of the mirror substrates done by Perkins Precision Development, Boulder (Colorado). Coating done by Advanced Thing Films.

and  $D = D_{J=5/2, m_j=-3/2}$ ). In order to measure which of these states the electron is in, the standard electron shelving technique is used. We perform this measurement for a ‘detection time’ (397 nm photon collection time) of 1500  $\mu\text{s}$ , which is sufficient to distinguish bright (scattering) and dark (non-scattering) ions with an error of less than 1%. The aforementioned process implements a projective measurement into the eigenstates of the  $\sigma_z$  basis (Pauli spin-1/2 operator).

To perform measurements in other bases e.g.  $\sigma_x$  ( $\sigma_y$ ), as required for full quantum state tomography, an additional  $\pi/2$  pulse on the  $S_{m_j=-1/2}$  to  $D_{m_j=-3/2}$  with a 0 ( $\pi/2$ ) phase is applied after the  $\pi$  pulse and before the 397 nm pulse, to rotate the ion-qubit measurement basis. The scheme of the experimental sequence is given in supplementary Figure S.5.

### C. State characterisation

To reconstruct the ion-photon state, a full state tomography of the two-qubit system is performed. On the photon polarisation qubit side, the state is projected to one of 6 states (horizontal, vertical, diagonal, anti-diagonal, right circular and left circular) by waveplates and polariser. This is equivalent to performing projective measurements in three bases described by the Pauli spin-1/2 operators. For example, horizontal and vertical are the eigenstates of the Pauli  $\sigma_z$  operator. On the ion qubit side, measurement is performed in the three Pauli bases as described in the previous section. From these measurements’ outcomes probabilities we reconstruct the 2-qubit state density matrix by linear search with subsequent Maximum Likelihood method [43]. The values of fidelity, concurrence and other measures presented in the Results section are calculated using reconstructed density matrices for each of the experiments. The error bars for all quantities provided in the Results section represent one standard deviation of distribution of these quantities over randomised set of data following the Monte-Carlo approach, for more details see [24].

### DATA AVAILABILITY

The data and code that support the findings of this study are available from the corresponding author upon reasonable request.

### ACKNOWLEDGMENTS

We thank the staff at IQOQI Innsbruck; Rainer Blatt for providing encouragement, laboratory space, and the environment and group support in which to develop our work; Daniel Heinrich, Klemens Schüppert, Tiffany Brydges, Christine Maier and Tracy Northup for their support. This work was supported by the START prize of the Austrian FWF project Y 849-N20, the Army Research Laboratory Center for Distributed Quantum Information via the project SciNet, the Institute for Quantum Optics and Quantum Information (IQOQI) of the Austrian Academy Of Sciences (OeAW) and the European Union’s Horizon 2020 research and innovation programme under grant agreement No 820445 and project name ‘Quantum Internet Alliance’. The European Commission is not responsible for any use that may be made of the information this paper contains.

### AUTHOR CONTRIBUTIONS

All authors contributed to the design, development and characterisation of the experimental systems. In particular, JS focused on the ion trap and optical cavity, MM on the photon conversion system, VKrc on the ion trap, HH on laser frequency stabilisation and VKru and BPL on all aspects. Experimental data taking was done by VKru, VKrc, MM and JS. Data analysis and interpretation was done by VKru, JS, MM and BPL. All authors contributed to the paper writing. The project was conceived and supervised by BPL.

- 
- [1] Kimble H.J. The quantum internet. *Nature* **453**, 1023 (2008).
  - [2] Wehner S., Elkouss D., Hanson R. Quantum internet: A vision for the road ahead. *Science* **362**, 6412 (2018).
  - [3] Ritter S., Nölleke C., Hahn C., Reiserer A., Neuzner A., Uphoff M., Mücke M., Figueroa E., Bochmann J., Rempe G. An elementary quantum network of single atoms in optical cavities. *Nature* **484**, 195 (2012).
  - [4] Moehring D.L., Maunz P., Olmschenk S., Younger K.C., Matsukevich D.N., Duan L.M., Monroe C. Entanglement of single-atom quantum bits at a distance. *Nature* **449**, 68 (2007).
  - [5] Hensen B., Bernien H., Dréau A.E., Reiserer A., Kalb N., Blok M.S., Ruitenberg J., Vermeulen R.F.L., Schouten R.N., Abellán C., Amaya W., Pruneri V., Mitchell M.W., Markham M., Twitchen D.J., Elkouss D., Wehner S., Taminiau T.H., Hanson R. Loophole-free bell inequality violation using electron spins separated by 1.3 kilometres. *Nature* **526**, 682 (2015).
  - [6] Maring N., Farrera P., Kutluer K., Mazzera M., Heinze G., de Riedmatten H. Photonic quantum state transfer between a cold atomic gas and a crystal. *Nature* **551**, 485 (2017).
  - [7] Radnaev A.G., Dudin Y.O., Zhao R., Jen H.H., Jenkins S.D., Kuzmich A., Kennedy T.A.B. A quantum memory with telecom-wavelength conversion. *Nature Physics* **6**, 894 EP (2010).

- [8] Albrecht B., Farrera P., Fernandez-Gonzalvo X., Cristiani M., de Riedmatten H. A waveguide frequency converter connecting rubidium-based quantum memories to the telecom c-band. *Nature Communications* **5**, 3376 (2014).
- [9] Dréau A., Tchegotareva A., Mahdaoui A.E., Bonato C., Hanson R. Quantum frequency conversion of single photons from a nitrogen-vacancy center in diamond to telecommunication wavelengths. *Phys. Rev. Applied* **9**, 064031 (2018).
- [10] Walker T., Miyanishi K., Ikuta R., Takahashi H., Vartabi Kashanian S., Tsujimoto Y., Hayasaka K., Yamamoto T., Imoto N., Keller M. Long-distance single photon transmission from a trapped ion via quantum frequency conversion. *Phys. Rev. Lett.* **120**, 203601 (2018).
- [11] Bock M., Eich P., Kucera S., Kreis M., Lenhard A., Becher C., Eschner J. High-fidelity entanglement between a trapped ion and a telecom photon via quantum frequency conversion. *Nature Communications* **9**, 1, 1998 (2018).
- [12] Siverns J.D., Hannegan J., Quraishi Q. Neutral atom wavelength compatible 780 nm single photons from a trapped ion via quantum frequency conversion. arXiv preprint arXiv:1801.01193 (2018).
- [13] Lo H.K., Curty M., Qi B. Measurement-device-independent quantum key distribution. *Phys. Rev. Lett.* **108**, 130503 (2012).
- [14] Schindler P., Barreiro J.T., Monz T., Nebendahl V., Nigg D., Chwalla M., Hennrich M., Blatt R. Experimental repetitive quantum error correction. *Science* **332**, 6033, 1059 (2011).
- [15] Linke N.M., Gutierrez M., Landsman K.A., Figgatt C., Debnath S., Brown K.R., Monroe C. Fault-tolerant quantum error detection. *Science Advances* **3**, 10 (2017).
- [16] Benhelm J., Kirchmair G., Roos C.F., Blatt R. Towards fault-tolerant quantum computing with trapped ions. *Nature Physics* **4**, 463 (2008).
- [17] Briegel H.J., Dür W., Cirac J.I., Zoller P. Quantum repeaters: The role of imperfect local operations in quantum communication. *Phys. Rev. Lett.* **81**, 5932 (1998).
- [18] Sangouard N., Dubessy R., Simon C. Quantum repeaters based on single trapped ions. *Phys. Rev. A* **79**, 042340 (2009).
- [19] Olmschenk S., Matsukevich D.N., Maunz P., Hayes D., Duan L.M., Monroe C. Quantum teleportation between distant matter qubits. *Science* **323**, 5913, 486 (2009).
- [20] Hucul D., Inlek I.V., Vittorini G., Crocker C., Debnath S., Clark S.M., Monroe C. Modular entanglement of atomic qubits using photons and phonons. *Nature Physics* **11**, 37 (2014).
- [21] Kómár P., Kessler E.M., Bishof M., Jiang L., Sørensen A.S., Ye J., Lukin M.D. A quantum network of clocks. *Nature Physics* **10**, 582 (2014).
- [22] Ilo-Okeke E.O., Tessler L., Dowling J.P., Byrnes T. Remote quantum clock synchronization without synchronized clocks. *npj Quantum Information* **4**, 1, 40 (2018).
- [23] Stute A., Casabone B., Schindler P., Monz T., Schmidt P.O., Brandstätter B., Northup T.E., Blatt R. Tunable ion-photon entanglement in an optical cavity. *Nature* **485**, 482 (2012).
- [24] Supplementary material of this paper.
- [25] Luo L., Hayes D., Manning T.A., Matsukevich D.N., Maunz P., Olmschenk S., Sterk J.D., Monroe C. Protocols and techniques for a scalable atom-photon quantum network. *Fortschr. Phys.* **57**, 11-12, 1133 (2009).
- [26] Hong C.K., Ou Z.Y., Mandel L. Measurement of subpicosecond time intervals between two photons by interference. *Phys. Rev. Lett.* **59**, 2044 (1987).
- [27] Krutyanskiy V., Meraner M., Schupp J., Lanyon B.P. Polarisation-preserving photon frequency conversion from a trapped-ion-compatible wavelength to the telecom c-band. *Applied Physics B* **123**, 9, 228 (2017).
- [28] Treiber R., Poppe A., Hentschel M., Ferrini D., Lorünser T., Querasser E., Matyus T., Hübel H., Zeilinger A. A fully automated entanglement-based quantum cryptography system for telecom fiber networks. *New Journal of Physics* **11**, 4, 045013 (2009).
- [29] Schindler P., Nigg D., Monz T., Barreiro J.T., Martinez E., Wang S.X., Quint S., Brandl M.F., Nebendahl V., Roos C.F., Chwalla M., Hennrich M., Blatt R. A quantum information processor with trapped ions. *New Journal of Physics* **15**, 12, 123012 (2013).
- [30] Wootters W.K. Entanglement of formation of an arbitrary state of two qubits. *Phys. Rev. Lett.* **80**, 2245 (1998).
- [31] Clauser J.F., Horne M.A., Shimony A., Holt R.A. Proposed experiment to test local hidden-variable theories. *Phys. Rev. Lett.* **23**, 880 (1969).
- [32] Lanyon B.P., Hempel C., Nigg D., Müller M., Gerritsma R., Zähringer F., Schindler P., Barreiro J.T., Rambach M., Kirchmair G., Hennrich M., Zoller P., Blatt R., Roos C.F. Universal digital quantum simulation with trapped ions. *Science* **334**, 6052, 57 (2011).
- [33] Wang Y., Um M., Zhang J., An S., Lyu M., Zhang J.N., Duan L.M., Yum D., Kim K. Single-qubit quantum memory exceeding ten-minute coherence time. *Nature Photonics* **11**, 10, 646 (2017).
- [34] Matsukevich D.N., Maunz P., Moehring D.L., Olmschenk S., Monroe C. Bell inequality violation with two remote atomic qubits. *Phys. Rev. Lett.* **100**, 150404 (2008).
- [35] Simon C., de Riedmatten H., Afzelius M., Sangouard N., Zbinden H., Gisin N. Quantum repeaters with photon pair sources and multimode memories. *Phys. Rev. Lett.* **98**, 190503 (2007).
- [36] Seri A., Lenhard A., Rieländer D., Gündoğan M., Ledingham P.M., Mazzer M., de Riedmatten H. Quantum correlations between single telecom photons and a multimode on-demand solid-state quantum memory. *Phys. Rev. X* **7**, 021028 (2017).
- [37] Chwalla M., Benhelm J., Kim K., Kirchmair G., Monz T., Riebe M., Schindler P., Villar A.S., Hänsel W., Roos C.F., Blatt R., Abgrall M., Santarelli G., Rovera G.D., Laurent P. Absolute frequency measurement of the  $^{40}\text{Ca}^+$   $4s^2s_{1/2} - 3d^2d_{5/2}$  clock transition. *Phys. Rev. Lett.* **102**, 023002 (2009).
- [38] Guggemos M., Heinrich D., Herrera-Sancho O.A., Blatt R., Roos C.F. Sympathetic cooling and detection of a hot trapped ion by a cold one. *New Journal of Physics* **17**, 10, 103001 (2015).
- [39] Hume D. Poster at international conference on atomic physics (icap), barcelona, 2018.
- [40] Chen J.S. Ticking near the Zero-Point Energy: Towards  $1 \times 10^{-18}$  Accuracy in  $\text{Al}^+$  Optical Clocks. Dissertation, University of Colorado Boulder (2017).
- [41] Schmidt P.O., Rosenband T., Langer C., Itano W.M., Bergquist J.C., Wineland D.J. Spectroscopy using quantum logic. *Science* **309**, 5735, 749 (2005).

- [42] Siegman A. Lasers. University Science Books (1986).
- [43] Hradil Z., Summhammer J., Rauch H. Quantum tomography as normalization of incompatible observations. Physics Letters A **261**, 1, 20 (1999).
- [44] Hood C.J., Kimble H.J., Ye J. Characterization of high-finesse mirrors: Loss, phase shifts, and mode structure in an optical cavity. Phys. Rev. A **64**, 033804 (2001).
- [45] Black E.D. An introduction to pound–drever–hall laser frequency stabilization. American Journal of Physics **69**, 1, 79 (2001).
- [46] Hainzer H. Laser Locking For Trapped-Ion Quantum Networks. Diplomarbeit, University of Innsbruck (2018).
- [47] Fleisher A.J., Long D.A., Liu Q., Hodges J.T. Precision interferometric measurements of mirror birefringence in high-finesse optical resonators. Phys. Rev. A **93**, 013833 (2016).
- [48] Stute A. A light-matter quantum interface: ion-photon entanglement and state mapping. Dissertation, University of Innsbruck (2013).
- [49] Maurer C., Becher C., Russo C., Eschner J., Blatt R. A single-photon source based on a single  $\text{Ca}^+$  ion. New Journal of Physics **6**, 1, 94 (2004).
- [50] Efron B., Tibshirani R. Bootstrap methods for standard errors, confidence intervals, and other measures of statistical accuracy. Statist. Sci. **1**, 1, 54 (1986).

## SUPPLEMENTARY MATERIAL

### I. Experimental details

#### I.A. Overview of ion-photon source

The cavity-ion-trap system developed for this project (and others) was recently constructed at the Innsbruck IQOQI building. The design is based on that of the system at the nearby University of Innsbruck that was used in [23]. The common design elements are a 20 mm long near-concentric optical cavity with a 3D linear-Paul ion trap hanging (rigidly) inside it. A key difference is that the present system’s cavity parameters are optimised to collect photons near-deterministically, as described in section II.B. Full details on the new cavity-integrated ion-trap system will be presented in the upcoming PhD theses of Josef Schupp and Vojtech Krcmarsky.

#### I.B. Cavity parameters

The optical cavity around the ion is near-concentric with a length  $l = 19.9057 \pm 0.0003$  mm and radii of curvature  $ROC = 9.9841 \pm 0.0007$  mm, determined from simultaneous measurements of the free spectral range (FSR) and higher-order TEM mode spacing (assuming identical mirror geometries) [42]. From this we calculate an expected cavity waist of  $\omega_0 = 12.31 \pm 0.07$   $\mu\text{m}$  and a maximum ion-cavity coupling rate of  $g_{max} = 2\pi \cdot 1.53 \pm 0.01$  MHz. At a wavelength of 854 nm, the finesse of the TEM<sub>00</sub> mode is  $\mathcal{F} = \frac{2\pi}{\mathcal{L}} = 54000 \pm 1000$ , with the total cavity losses  $\mathcal{L} = T_1 + T_2 + L_{1+2} = 116 \pm 2$  ppm,

determined from measurements of the cavity ringdown time  $\tau_C = \frac{\mathcal{F}}{\pi} \cdot \frac{l}{c_0}$ , with  $c_0$  the speed of light in vacuum. From this one can calculate the cavity linewidth  $2\kappa = 2\pi \cdot 140 \pm 3$  kHz,  $\kappa$  being the half-width at half maximum.

The transmission  $T_{1,2}$  of our cavity mirrors<sup>3</sup> was verified by applying the method described in [44], yielding  $T_1 = 2.2 \pm 0.3$  ppm,  $T_2 = 97 \pm 4$  ppm, such that the combined mirror losses from scattering and absorption  $L_{1+2} = 17 \pm 5$  ppm.

From this one can calculate the probability that a photon inside the cavity exits through mirror  $T_2$  (designated output mirror) as  $P_{out}^{max} = T_2 / (T_1 + T_2 + L_{1+2}) = 0.83 \pm 0.03$ .  $P_{out}^{max}$  is therefore the maximum photon collection probability from the ion in our system (with the current mirrors). The system of [23] has  $P_{out}^{max} = 0.16$ .

The cavity length is stabilised via the Pound-Drever-Hall (PDH) method [45] to a laser at 806 nm with a linewidth on the order of 1 kHz [46]. The 806 nm wavelength lies far from any transition in  $^{40}\text{Ca}^+$  to minimise AC Stark-shifts on the ionic transitions. The cavity is locked to a TEM<sub>01</sub> mode and the ions sits in the central intensity minimum to further minimise AC Stark shifts.

The cavity waist is centred on the ion via course tuning of a 3D piezo stick-slip translation-stage system (Attocube). Before experiments, photon generation efficiency is optimised by placing the ion in a cavity anti-node. This is done via fine tuning of the cavity position along its axis by applying a small bias voltage to the corresponding piezo stage.

Some key challenges that were overcome to realise our cavity parameters are now briefly described. A complete presentation will be part of the upcoming thesis of Josef Schupp. First, the superpolishing of the surfaces of such tightly curved (10 mm ROC) mirror substrates seems not to be a commercially available process as standard and we are therefore grateful to Perkins Precision, Boulder, who did it as a custom job, achieving an RMS roughness of  $1 \pm 0.2$  Å and 1.5 ppm scattering losses on a test piece from the batch. Second, mirror coating via ion beam sputtering was performed by Advanced Thin Films, leading to a mirror pair with total scattering and absorption losses of 9 ppm in our near-concentric configuration. Third, the observed birefringence of cavities built using these mirrors could be minimised by rotating mirror pairs w.r.t. each other, leading to a sub-linewidth ( $2 \cdot \kappa$ ) splitting of  $14 \pm 2$  kHz in the final cavity (measured by the method of [47]). The fourth step involved a multi-stage procedure to glue the mirrors into position to achieve the near-concentric cavity (the mirrors are glued into metal rings, in turn glued to piezos for cavity-length stabilisation, in turn glued to a rigid metal spacer spanning the cavity length: the only tuneable parameter once

<sup>3</sup> Polishing of the mirror substrates done by Perkins Precision Development, Boulder (Colorado). Coating done by Advanced Thing Films.

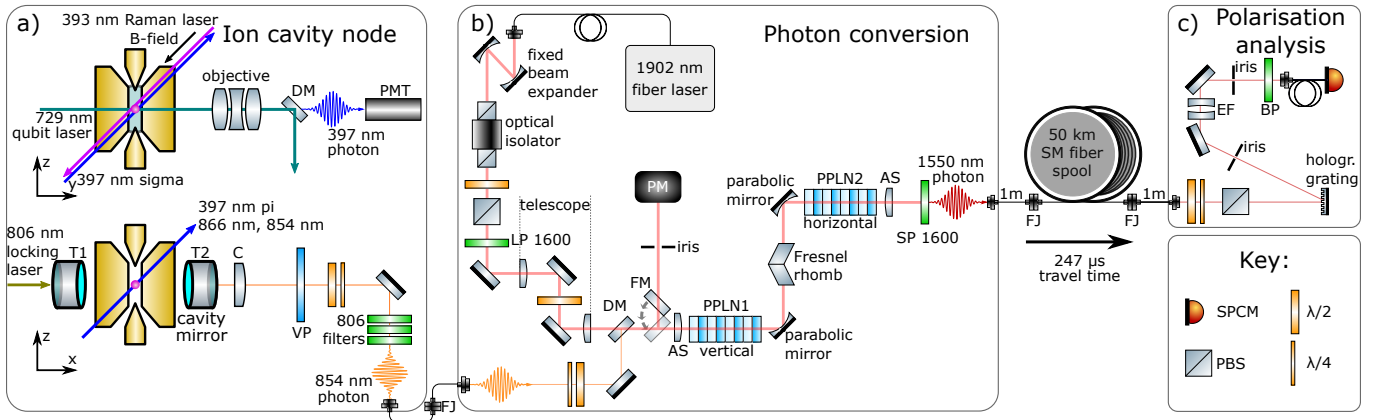


**FIG. S.4. Detailed experimental diagram.** **a) Ion cavity node.** A single atomic ion (red sphere) in the centre of both a 3D radio-frequency (RF) linear Paul trap (gold electrodes) and an optical cavity. Two smaller electrodes are ‘end-caps’ held at DC voltage. Two larger electrodes are held at RF, two additional larger electrodes exist but are not shown. Two cross sections are presented. The top view looks along the cavity axis and shows: the  $\approx 4$  Gauss DC magnetic field (quantisation axis) generated by rings of permanent magnets fastened to the vacuum chamber (not shown): the circularly-polarised Raman laser for generating cavity 854 nm photons: the 729 nm laser for ion-qubit manipulation and measurement **II.D**: a custom objective (NA = 0.289,  $f = 66.8$  mm, lying in an inverted viewport) for collecting spontaneously scattered 397 nm photons for ion-qubit state detection (PMT: Photo multiplier tube). The circularly polarised 397 nm sigma beam is used for optical pumping. Bottom view: perpendicular to the cavity axis. Following a Raman pulse, a cavity 854 nm photon exits via mirror with transmission T2 with probability  $\geq 0.5 \pm 0.1$  **III.A**. The photon then passes the following elements: in-vacuum collimating lens C: vacuum chamber viewport VP (CF40, Fused Silica, SS316LN, UK atomic energy authority); waveplates (for polarisation analysis of 854 nm photon **IV**); 3 filters (Semrock,  $2 \times$  FF01-834/LP-25,  $1 \times$  FF01-850/10-25) to remove 806 nm laser light to which cavity length is continuously and actively stabilised **II.B**). The 854 nm photon is then coupled into single mode (non-polarisation maintaining) fibre leading to the photon conversion setup (total length 10 m with fibre-fibre joiner, FJ). The 397 nm pi beam is used for Doppler cooling and ion-qubit state detection. **b) Photon conversion.** The injected 854 nm photon passes waveplates (used for system setup with classical light) and is overlapped with 1 W of 1902 nm laser light (Tm-doped fibre laser, AdValue Photonics: AP-SF1-1901.4-01-LP) on a dichroic (DM, Layertec 103472) and free-spaced coupled into one of the ridge waveguides of PPLN1 using an asphere (AS - 11 mm, Thorlabs A220TM, positioned by XYZ translation stage). Waveguides are temperature stabilised with peltier systems. Gold parabolic mirrors are used for simultaneous focusing/collimation of all fields ( $f = 15$  mm, Thorlabs MPD00M9); Fresnel Rhomb (FR600HM, Thorlabs) 1902 nm input path includes: beam expander (Thorlabs, BE02R) to reduce the beam diameter so as to fit an optical isolator (Thorlabs IO-4-2050-HP): waveplate and polariser for total power control; LP 1600 nm - longpass filter (Edmund Optics 84 - 680) to reduce 1500 nm photons produced directly from fiber laser: simple telescope to optimise coupling efficiency into waveguide. A flip mirror (FM) before PPLN1, and subsequent classical power meter (PM) allows for verifying spatial overlap of 1902 nm and 854 nm (with 854 nm classical light). SP 1600 nm - shortpass filter (OD5 at 1902 nm, Edmund Optics 84 - 656). 50 km fibre spool (Corning SMF-28 ultra, Fiontec). **c) Polarisation analysis.** hologr. grating - volume holographic Bragg grating (reflection bandwidth 0.2 nm [25 GHz], 95% reflection, OptiGrate) EF - air-spaced Fabry-Pérot cavity (250 MHz linewidth, 12.5 GHz free spectrum range, peak transmission 95% at 1550 nm, extinction  $10^3$ , SLS optics); BP - bandpass 1550 nm filter (12 nm bandwidth and 95% transmission, Thorlabs FBH-1550). The total conversion efficiency given in the main text ( $25 \pm 0.02$  %) is the probability of getting a 1550 nm photon (from the ion) in the fibre immediately before the single photon counting module (SPCM, InGaAs ID230, IDQuantique), given a fibre-coupled 854 nm input photon in the input fibre to the conversion setup, in the case where the 50 km fibre spool is removed and the waveplates in the polarisation analysis are set to maximise subsequent PBS transmission.

glued is the cavity length). The fifth and final key step was for the cavity to survive the ion-trap chamber vacuum baking process, which was achieved by baking at 80 °C, limited by the glass transition temperature of the cavity glue.

### *I.C. Polarisation maintaining single photon conversion setup*

A detailed schematic of the photon conversion system is presented in Figure S.4. Details about the operation

and characterisation of the system (using classical 854 nm laser light) can be found in [27]. Figure S.4 provides more details about the pump laser path, the location of the 50 km fibre spool w.r.t. to the filtering network and the final filters employed (a long pass filter, with 1440 nm cutoff, has here been removed after photon conversion since the 50 km fibre spool performs an equivalent task of attenuating weakly phased-matched frequency-doubled pump laser light). We now provide a short summary of the conversion setup.

Difference frequency generation (DFG) is used to convert a 854 nm photon to 1550 nm via a  $\chi^{(2)}$  nonlinearity

in a 48 mm long PPLN ridge waveguide-integrated chips<sup>4</sup>  $(854 \text{ nm})^{-1} - (1902 \text{ nm})^{-1} \approx (1550 \text{ nm})^{-1}$ . Two chips are used in series to convert orthogonally-polarisation components of the 854 nm photon sequentially (while the ridge guides support all polarisations, they each convert only one polarisation component). Specifically, in our system, each waveguide converts the vertically-polarised components of the fields. The Fresnel rhomb between the chips (equivalent to a broadband half-waveplate) acts to rotate horizontal to vertical polarisations of all three fields, such that the second chip converts the orthogonal polarisation components to the first chip (see description in [27]).

200 mW of vertically-polarised 1902 nm pump is required in each PPLN for maximum conversion efficiency. To achieve this we send in a total of  $\approx 1 \text{ W}$  of 1902 nm light at the input to PPLN1, with polarisation set to achieved a balanced and maximum conversion efficiency in each PPLN chip.

For extracting the single telecom photon at the output, a filter network consisting of a short-pass (OD5 for 1902 nm, cutoff 1600 nm) for reducing the pump power, a volume holographic Bragg grating (bandwidth 0.2 nm) and an etalon (bandwidth 250 MHz) for reducing the 1550 nm noise photons from anti-Stokes Raman scattering, is used.

#### I.D. Pulse sequence for 50 km experiment

Figure S.5 shows the laser pulse sequence for the 50 km ion-photon entanglement experiment.

## II. Photon distribution efficiency

In this section information is presented on the efficiency with which photons are distributed in the 50 km experiment and the sources of photon loss.

#### II.A. Current setup efficiency

In the 50 km experiment, the total probability that a Raman photon generation pulse leads to a photon click after 50 km is  $5.3 \times 10^{-4}$  (after summing up the outcomes of all polarisation projections).

The total probability of obtaining an on-demand free-space photon out of the ion vacuum chamber is  $P_{out} = 0.5 \pm 0.1$ . This value is inferred from the measured efficiency with which we detect single-mode fibre-coupled (ion-entangled) photons at 854 nm (before the conversion stage), after correcting for the measured 1st fibre-coupling stage efficiency and the known 854 nm photon

detector efficiency. The uncertainty in  $P_{out}$  is dominated by the uncertainty in the 1st fibre-coupling stage efficiency, which could be reduced in future.

The overall efficiency of the frequency-conversion setup, including spectral filtering, is  $0.25 \pm 0.02$ , measured with classical 854 nm light. For a detailed description see [27]. A short overview of the contributing photon losses are summarised in table I. Multiplying all the transmissions together leads to a total expected probability of detecting the photon after 50 km of  $(6.5 \pm 1.5) \times 10^{-4}$ , which is consistent to within one standard deviation with the measured value of  $5.3 \times 10^{-4}$ .

Location in the photon path	Efficiency
On demand photon out of cavity $P_{out}$	$0.5 \pm 0.1$
1 <sup>st</sup> single-mode fibre coupling	$0.5 \pm 0.1$
Telecom conversion stage (& filtering)	$0.25 \pm 0.02$
50 km fibre transmission	$0.104 \pm 0.005$
Telecom photon detector efficiency	$0.10 \pm 0.01$
Expected 50 km detection probability	$(6.5 \pm 1.6) \times 10^{-4}$

TABLE I. Photon losses in our 50 km photon distribution experiment. See Fig. 1 in the main paper for the respective locations in the experimental setup.

A total 50 km detection probability of 0.01 should be straightforward to achieve. For example, telecom photon detectors with efficiencies of  $> 0.8$  and dark count rates of  $< 5 \text{ cps}$  are now commercially available. Since taking the data presented in this paper, we have improved the 1st fibre-coupling stage efficiency to  $0.9 \pm 0.1$  and further improvements should be possible. These changes alone are sufficient to achieve a total 50 km efficiency above 0.01.

The efficiency  $P_{out}$  in our setup is limited by losses in our mirror coatings to  $P_{out}^{max} = 0.83 \pm 0.03$ . Numerical simulations show that it should be possible to reach this value in our experiment [49] (that is, the probability of the ion emitting into the cavity mode could be near 100%) and recent experiments with our system show that  $P_{out} \approx 0.7$  is possible by cooling the ion close to the axial-mode ground state (and thereby enhancing the coupling strength of the cavity-mediated Raman transition, in comparison to the detrimental  $P_{3/2}$ -state spontaneous scattering rate).

Finally, the achieved photon conversion stage efficiency is predominantly limited by unwanted excitation of higher-order spatial modes in the involved PPLN ridge waveguides [27]. A total device efficiency of 0.5 should be within reach with more careful attention to coupling into the guides and minimising other passive optical losses (e. g. avoiding unnecessary fiber joints). Combing all of the aforementioned improvements would lead to a total 50 km detection probability of nearly 0.03, close to the 50 km fibre transmission of 0.1.

Note that lower loss telecom fibres than the one used here are available (0.16 dB/km, Corning SMF-28 ULL)

<sup>4</sup> produced by NTT electronics

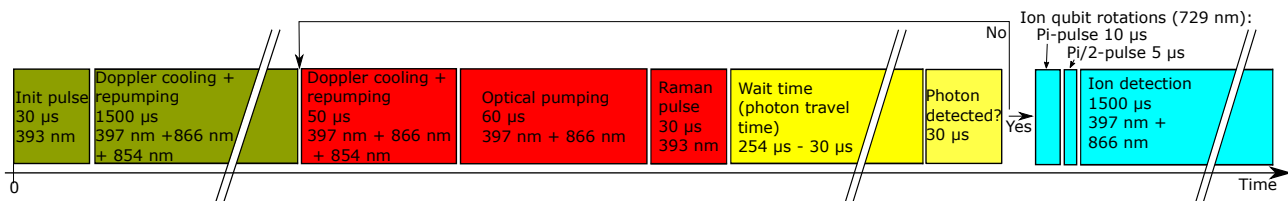


FIG. S.5. **Laser pulse sequence for the experiment.** The starting sequence (shown in green) consists of an initialisation laser pulse for intensity stabilisation and Doppler cooling. The loop (shown in red and yellow) consists of additional Doppler cooling, optical pumping, a (photon generation) Raman pulse, a wait time as the photon travels through the 50 km fiber to the detector and a detection window. If the photon detector clicks during within this window, ion qubit manipulation and state detection (shown in blue) are performed, otherwise the loop repeats.

with a corresponding 50 km transmission of 0.16 and any improvement in fibre technology will further increase that value.

### III. State characterisation

To reconstruct the ion-photon state, a full state tomography of the two-qubit system is performed. On the photon polarisation qubit side, the state is projected to one of 6 states (horizontal, vertical, diagonal, anti-diagonal, right circular and left circular) by waveplates and polariser. This is equivalent to performing projective measurements in three bases described by the Pauli spin-1/2 operators. For example, horizontal and vertical are the eigenstates of the Pauli  $\sigma_z$  operator. On the ion qubit side, measurement is performed in the three Pauli bases as described in section II.D.

For each of the 9 possible joint measurement bases (choice of photon basis and ion basis), the numbers of events corresponding to one of the four possible outcomes of these 2-qubit measurements are considered. We then divide the number of events recorded for each outcome by the total number of events recorded for the given basis (divide each number by the sum of four) and thus obtain estimates of the outcome probabilities. These probabilities are used to reconstruct the 2-qubit state density matrix by linear search with subsequent Maximum Likelihood method [43]. The values of fidelity, concurrence and other measures presented in the main text are calculated using reconstructed density matrices for each of the experiments.

For statistical analysis (determining error bars in quantities derived from the reconstructed density matrix), the Monte-Carlo approach was implemented [50]. Briefly, we numerically generate  $M = 200$  sets of 36 event numbers with Poissonian distribution and mean value equal to the experimental value for each of the 36 possible outcomes. From these simulated event numbers we derive simulated outcome probabilities, the same way as we do for the experimental counts. Then we reconstruct  $M$  density matrices for this simulated data and for each one we calculate the quantities of interest (fidelity, concurrence). The error bars given in the main text represent one stan-

dard deviation in the widths of the distributions of these quantities over  $M$  simulated data sets.

We quantify the state quality in terms of fidelity  $F^m$  defined as  $F^m = \left[ \text{Tr} \sqrt{\sqrt{\rho_{exp}} \rho_{max.ent.} \sqrt{\rho_{exp}}} \right]^2$ , where  $\rho_{exp}$  is the density matrix, reconstructed from the experiment data and  $\rho_{max.ent.}$  is the density matrix of the nearest maximally-entangled pure state. This nearest state is found by exposing a perfect Bell state to single qubit unitary rotations and searching for a state providing the best fidelity with the experimentally obtained one.

### IV. Imperfections in the entangled state

Sources of infidelity in the experimentally-reconstructed ion-photon entangled state given in the main text are now analysed. As we will show, the 50 km ion-photon state infidelity can be accounted for (to within statistical uncertainty) by taking into account background detector counts and imperfections in the initial ion-854 nm photon state output from the ion-trap.

Three independent experiments are performed, corresponding to state tomography of the ion-photon state at three different points in the path: First the ion-854 nm photon state immediately at the cavity output (using free space polarisation analysis and two single-mode fibre-coupled 854 nm photon detectors, one at each port of a polarising beam splitter): Second, the ion-1550 nm photon state immediately after conversion (with only a 1 m telecom fibre), referred to as 0 km distance: Third, the ion-1550 nm photon state after 50 km travel (as presented in the main text). The reconstructed state fidelities, with maximally entangled states, are presented in table II (bottom row ‘Experiment’).

The effect of background photon detector counts is analysed (defined as a detector click that didn’t result from a photon from the ion). For this, the background count rate is extracted from the measured counts in the tomography experiments by looking far outside the time window in which the ion-photon arrives, giving  $2 \pm 0.1$  cps for the 1550 nm photon at 50 km and  $10 \pm 1$  cps for the 854 nm photon, which are both in agreement with the telecom ( $1.9 \pm 0.15$  cps) and 854 nm ( $10.1 \pm 0.9$  and  $10.8 \pm 1$  cps) de-

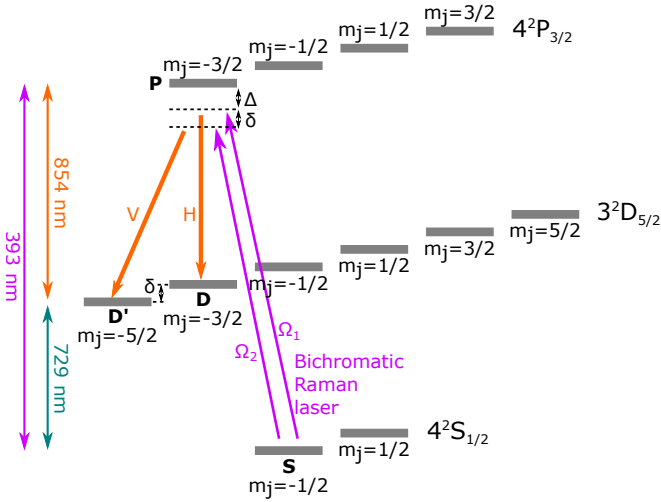


FIG. S.6. Relevant energy level scheme of  $^{40}\text{Ca}^+$ . The cavity-mediated Raman transition (CMRT) is shown, for generating an 854 nm photon that is polarisation entangled with the final electronic state of the ion. For details on the CMRT see the publication [23] and the PhD thesis [48]. In summary, following optical pumping, the ion (single outer valence electron) begins in the state  $S$ . A bichromatic 393 nm Raman pulse is applied with a frequency splitting equal to that of the  $D$ - $D'$  states. The bichromatic field and an optical cavity locked to the 854 nm transition generate two Raman processes, leading to the total transformation  $|S, 0\rangle \rightarrow 1/\sqrt{2}(|D, H\rangle + |D', V\rangle)$ , where  $0$ ,  $H$  and  $V$  are: 0 photons, a single horizontally-polarised and a single vertically-polarised photon in the cavity, respectively. The aforementioned polarisations are the projections into the optical cavity axis (perpendicular to the magnetic field). The relative amplitude of the two terms in the entangled superposition state are balanced in a separate calibration stage (see [48]), controlled via the relative intensities of the two frequency components in the Raman beam. The phase of the entangled state can be controlled via the relative phase of the two frequency components in the Raman beam. The detuning  $\Delta = 409 \pm 10$  MHz. In experiments we set the Rabi frequencies  $\Omega_1$  and  $\Omega_2$  so as to produce both polarisations with equal probabilities, as described in [23]. The total AC Stark shift exerted by the bichromatic Raman laser on the  $S$  state was measured (via 729 nm spectroscopy) to be  $AC = 2\pi \cdot (1.14 \pm 0.05)$  MHz, where  $AC = \Omega_1^2/4\Delta + \Omega_2^2/4(\Delta + \delta)$ .

tectors' dark count rates (measured independently). For the 1550 nm photon at 0 km we get  $4 \pm 0.1$  cps, where the additional 2 cps background is produced by the photon conversion pump laser anti-Stokes Raman scattering which was reported in [27]. Note that this added noise is attenuated at the same rate as the photons from the ion

over the 50 km, and so becomes a small contribution to the background compared to the intrinsic detector dark counts (which do not attenuate over distance).

The infidelity that the background counts would contribute when applied to a perfect maximally-entangled Bell state is simulated numerically. Specifically, the expected background count probability in our photon time-window is added to the expected measurement outcome probabilities for a perfect state, then a new 'noisy' state density matrix is reconstructed via Maximum Likelihood tomography. We call this approach 'Model 1', which simulates the effect of measured background counts only, and find that it explains the majority of the infidelity in the 50 km state (see Table II).

In addition to the background counts, Model 2 takes the measured imperfect 854 nm ion-photon state into account. That is, the tomographically reconstructed ion-854 nm-photon state is used as the state to which background counts are added as with Model 1. The results, shown in table II, show that background counts and imperfections in the initial 854 nm state explain the state infidelities to within statistical uncertainty.

Regarding infidelities in the initial ion-854 nm photon state: the fidelity in this case is limited by the state purity ( $\text{Tr}(\rho^2) = 0.94 \pm 0.01$ , where  $\rho$  is the 854 nm reconstructed state) meaning that only the imperfections leading to decoherence (or effective decoherence) need be considered. Possible error sources include errors in the 729 nm laser pulses used to determine the ion measurement basis, decoherence of the ion-qubit due to e.g. fluctuating magnetic fields and relative intensity fluctuations of the two frequency components in the Raman drive leading to a mixture of different states over the duration of the experiment. Identifying the size and relative contribution of these errors is beyond the scope of this work. The achieved fidelity at 854 nm is similar to that achieved in [23].

Fidelity, %	854nm@0km	1550@0km	1550@50km
Model 1	99.5	96	86
Model 2	-	93	83
Experiment	$96.7 \pm 0.6$	$92 \pm 2$	$86 \pm 3$

TABLE II. Comparison of modelled and measured ion-photon entangled state fidelities. Model 1: ideal Bell state subjected to background counts during photon qubit measurement. Model 2: Experimentally reconstructed 854 nm state affected by background counts.